First Constraints on Dark Photon Dark Matter with Superconducting Nanowire Detectors in an Optical Haloscope

Jeff Chiles,[1,*] Ilya Charaev,[2,*] Robert Lasenby,[3] Masha Baryakhtar,[4,5] Junwu Huang,[6] Alexana Roshko,[1] George Burton,[1] Marco Colangelo,[2] Ken Van Tilburg,[4,7] Asimina Arvanitaki,[6] Sae-Woo Nam,[1] and Karl K. Berggren[2]

[1] *National Institute of Standards and Technology, 325 Broadway, Boulder, CO 80305*
[2] *Massachusetts Institute of Technology, 50 Vassar Street, Cambridge, MA 02139, USA*
[3] *Stanford Institute for Theoretical Physics, Stanford University, Stanford, CA 94305, USA*
[4] *New York University CCPP, New York, NY, 10003, United States*
[5] *Department of Physics, University of Washington, Seattle WA 98195, USA*
[6] *Perimeter Institute for Theoretical Physics, Waterloo, Ontario, N2L 2Y5, Canada*
[7] *Center for Computational Astrophysics, Flatiron Institute, New York, NY 10010, USA*

Uncovering the nature of dark matter is one of the most important goals of particle physics. Light bosonic particles, such as the dark photon, are well-motivated candidates: they are generally long-lived, weakly-interacting, and naturally produced in the early universe. In this work, we report on LAMPOST (Light A' Multilayer Periodic Optical SNSPD Target), a proof-of-concept experiment searching for dark photon dark matter in the $\sim$ eV mass range, via coherent absorption in a multilayer dielectric haloscope. Using a superconducting nanowire single-photon detector (SNSPD), we achieve efficient photon detection with a dark count rate (DCR) of $\sim 6 \times 10^{-6}$ counts/s. The observed count rate in our detector differed insignificantly from a reference SNSPD, enabling our prototype experiment to set new limits for the dark photon dark matter kinetic mixing parameter $\epsilon \lesssim 10^{-12}$ and find no evidence for dark photon dark matter over a mass range of $\sim$ 0.7-0.8 eV (photon wavelength $\sim$ 1550-1770 nm). This performance demonstrates that, with feasible upgrades, our architecture could probe significant new parameter space for dark photon and axion dark matter in the meV to 10 eV mass range.

I. Introduction

Dark matter (DM), a form of non-relativistic matter that amounts to $\sim 25\%$ of the energy budget of the universe, is by now the conservative explanation for a wealth of astrophysical and cosmological data that cannot be accommodated within the Standard Model (SM) of particle physics [1, 2]. However, all of our evidence for DM is via its gravitational interactions on large scales, which is compatible with a very wide range of microphysical models.

Light, weakly-coupled new bosons are a well-motivated class of DM candidates [3–6]. Light scalar, pseudoscalar, and vector particles arise in many SM extensions and are generally weakly coupled, long-lived, and difficult to detect [7–13]. These bosonic DM candidates are also automatically produced in the early universe assuming a period of cosmic inflation [5, 6]. For vector DM, the abundance today depends on the inflationary Hubble scale [6], and can yield the measured DM abundance for DM masses $\gtrsim 5 \times 10^{-5}$ eV given current constraints on the inflationary scale [14]. The detection of a vector DM particle at the eV scale would point to a Hubble scale of 5×10^{12} GeV, otherwise unreachable in any laboratory experiment or astrophysical observation.

The simplest and least-constrained vector DM model is the dark photon, characterized by the 'kinetic mixing' interaction with the photon [15],

$$\mathcal{L} \supset -\frac{1}{4}F_{\mu\nu}F^{\mu\nu} - \frac{1}{4}F'_{\mu\nu}F'^{\mu\nu} - \frac{1}{2}\epsilon F_{\mu\nu}F'^{\mu\nu} + \frac{1}{2}m_{A'}^2 A'^2 \quad (1)$$

where $F_{\mu\nu}$ and $F'_{\mu\nu}$ are the field strengths of the photon and the dark photon, respectively, and A' is the dark photon field. The dark photon mass $m_{A'}$ and kinetic mixing parameter $\epsilon \ll 1$ define the DM parameter space.

Similarly to a photon, the leading interaction between dark photon DM and a detector is the *absorption* of the DM particle [16, 17]. The entire rest mass energy $m_{A'}c^2$ can be captured, in contrast to scattering, which deposits at most the kinetic energy $m_{A'}v^2$ in direct detection experiments [18] (where $v \sim 10^{-3}c$ is the galactic DM velocity and c is the speed of light). This motivates new experimental schemes for detection of light bosonic DM. In this work, we focus on the efficient conversion of dark photon DM to near-IR photons.

To convert a non-relativistic dark photon into a relativistic photon of the same frequency, the target must compensate for the mismatch in momentum. This can be achieved using a stack of dielectric layers

* Both authors contributed equally to this work. jeffrey.chiles@nist.gov, charaev@mit.edu.

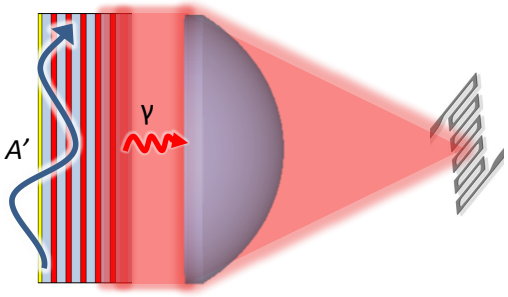

Figure 1. Sketch of the LAMPOST concept. The dark photon dark matter field A' converts to photons in a layered dielectric target. These photons are focused by a lens onto a small, low-noise SNSPD detector.

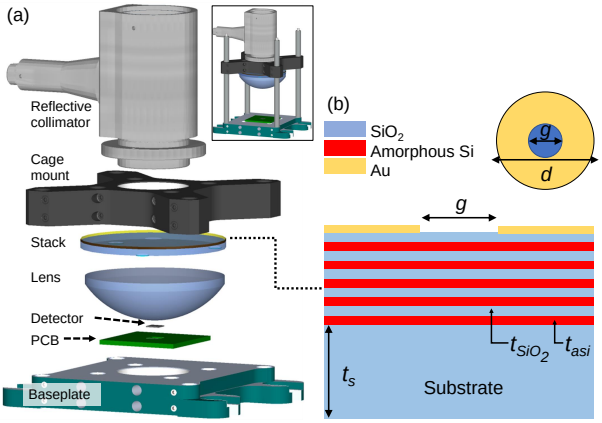

Figure 2. The LAMPOST prototype haloscope apparatus. (a) Exploded view with element details. Inset: assembled view. b) Schematic cross-sectional and top-views of the dielectric stack target responsible for DM-signal photon conversion, with designed values of different dimensions, g: Aperture diameter, 10 mm; d: Wafer diameter, 52 mm; t_s: Substrate thickness, 525 μm; t_{asi}: Amorphous silicon layer thickness, ∼292 nm; t_s: SiO_2 layer thickness, ∼548 nm. See Supplementary Materials for details of the film characterization.

with different indices of refraction, whose thicknesses are on the scale of the photon's wavelength [16, 19–22]. In such a structure, dark photon DM at the corresponding frequency can convert coherently to photons, with the conversion rate increasing as the number of layers squared (see Fig. 1 for the detector concept).

Due to the small DM velocity, the converted photons are emitted within $\sim 10^{-3}$ rad of the normal vector to the layers. This allows them to be focused down to an area $\sim 10^{-6}$ smaller than that of the layers, permitting the use of small, highly sensitive detectors [16, 17, 19]. Superconducting nanowire single-photon detectors (SNSPDs) have demonstrated, in separate experiments, ultralow dark count rates necessary to detect rare signal events (10^{-6} Hz), active areas large enough to collect the focused light ($\gtrsim 0.1\,\mathrm{mm}^2$), near-unity detection efficiency, and sensitivity to photons in the wide energy range of 0.1 to 10 eV [23–26]. These properties make SNSPDs well-suited to the unique requirements of this project.

In this work, we present the first results from the LAMPOST (Light A' Multilayer Periodic Optical SNSPD Target) experiment with 180 hours of data collection. We describe the construction and characterization of the multi-layer dielectric haloscope target and the SNSPD detector. Our simple and inexpensive prototype constrains new dark photon DM parameter space at masses $\sim$ 0.7-0.8 eV (corresponding to photon wavelengths $\sim$ 1550-1770 nm) with less than a week of run time. We outline potential improvements to further increase the experimental reach and allow this architecture to probe significant new parameter space in the near future.

II. Experimental setup

The dielectric stack, or target, generates the signal photons of interest. As discussed in [16], a useful configuration is a 'half-wave' stack, in which the stack's layers have alternating refractive indices $n_1, n_2, n_1, n_2, \ldots$ and thicknesses $d_1, d_2, d_1, d_2, \ldots$, with $n_1 d_1 = n_2 d_2$. The thicknesses and indices are chosen for light at the signal wavelength of interest to acquire π phase upon transmitting through each layer. In such a material, dark photon DM with frequency $\omega \simeq n_i d_i/\pi$ can convert coherently to photons, with conversion rate scaling as the square of the number of layers (for stacks thinner than the DM coherence length). We utilise alternating layers of amorphous silicon and silica, deposited on top of a ~ 0.5 mm thick silica substrate.

The dielectric stack is integrated and aligned with several optomechanical elements and a lens (focal length of 50 mm) to focus the signal onto the primary SNSPD. The structure is illustrated in the right-hand panel of Fig. 2. A reference SNSPD, nominally identical to the first, is placed nearby to provide a background count rate estimate, since no signal photons impinge on the reference detector. The entire apparatus is contained inside a light-tight box. During data collection, counts from the primary and reference SNSPD are compared: a DM signal would correspond to an excess of counts in the primary SNSPD, as compared to the reference.

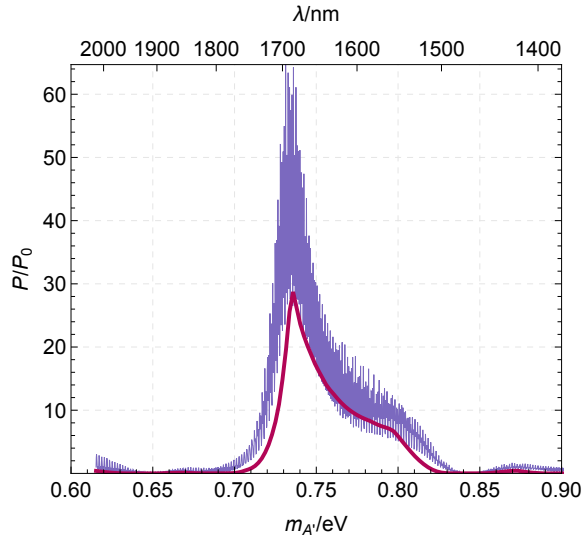

Figure 3. Calculated time-averaged power P absorbed from dark photon DM with mass $m_{A'}$ by the layered target, normalised to the power P_0 absorbed by a uniform mirror. The thin purple curve shows the power absorbed by a target with parameters given by their respective measured central values, while the magenta curve shows the minimum power obtained by varying the parameters within measurement uncertainties (see Methods). The substrate thickness is assumed to physically vary by $\gtrsim 10\,\mu$m over the target area; this accounts for the magenta curve sometimes falling above the purple curve of constant substrate thickness.

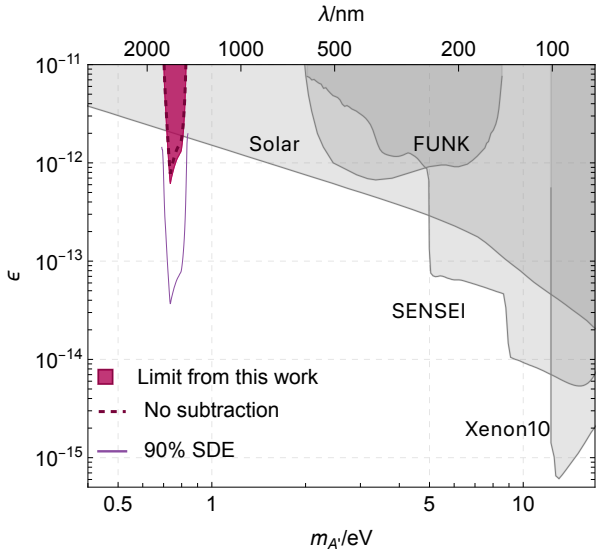

Figure 4. LAMPOST constraints on dark photon DM with mass $m_{A'}$ and kinetic mixing ϵ. The magenta shaded region shows the 90% limit set by our experiment. The dashed curve shows the 90% limit obtained without background subtraction. The thin purple curve corresponds to the reach of an equivalent experiment with an improved SDE of 90%. Existing limits on dark photon DM from the FUNK [29], SENSEI [30] and Xenon10 [31] experiments and from the non-detection of Solar dark photons by Xenon1T [32] are shown in gray.

The calculated converted power P per unit target area A, as a function of dark photon mass, is shown in Fig. 3. This power is normalised to the time-averaged power converted by a simple mirrored surface, $P_0/A = \frac{2}{3}\epsilon^2\rho_{\rm DM}$, where $\rho_{\rm DM}$ is the local DM energy density. Our layered target enhances the conversion rate by up to a factor ~ 30 times that of a mirror target [27–29], even taking into account measurement uncertainties. See Methods for more details.

After assembling the dielectric stack and the SNSPD as in Fig. 2, we combine simulated and experimentally measured factors to obtain a well-bounded number for the system detection efficiency (SDE), which captures all known sources of loss from the point of signal photon generation in the stack to the generation of photon count events in the SNSPD. Overall, we achieve a lower bound for the SDE of 0.32% in our system. The loss is dominated by the optical collection efficiency (OCE) of 2.1%; this factor considers the fraction of photons impinging on the detector after exiting the stack. See Methods for further details and discussion.

III. Results

Over a 180 hour exposure, the reference SNSPD registered 5 counts, while the primary SNSPD registered 4 counts. This is clearly compatible with similar noise rates and no DM signal in the haloscope detector. As discussed in the Supplementary Material, we set a 90% confidence limit on the kinetic mixing ϵ, corresponding to the value that would give 5 expected signal events in 180 hours. Figure 4 shows this limit, derived by minimising over measurement uncertainties as described in Section V, compared to existing bounds [32]. We assume a local DM density of $0.4\,\text{GeV}\,\text{cm}^{-3}$, with a standard truncated Maxwell-Boltzmann velocity distribution [33].

We expect the responses of the reference and primary SNSPDs to be similar (see Supplementary Fig. 12); however, this is not guaranteed as fabrication defects could lead to different noise rates. To be maximally conservative, we can ask what signal rates would be incompatible with 4 counts in the primary detector, even assuming that all of these were DM events. At the 90% confidence level, this corresponds to ≥ 8 expected signal events. This limit is shown as the dashed curve in Fig. 4, showing that even without background subtraction, we constrain similar parameter space.

Fig. 4 shows that our prototype detector constrains previously unexplored DM parameter space in the mass range $0.7-0.8\,\mathrm{eV}$. This is achieved with only 5 target layer pairs, relatively low SDE, and measurement uncertainties.

IV. Discussion

There are several clear directions toward extending the experimental reach beyond the prototype. The first is improving the OCE from its current value of 2.1%, which suffers from a combination of optical aberrations and reflective losses. Considering the trade-offs, we selected a system design that would provide sufficient signal over a reasonable timeframe while minimizing the risk of undetected misalignment from tilt or thermo-mechanical shifts. In the future, spherical aberration and total internal reflection losses could be mitigated with a longer-focal length lens, reaching 93% OCE (see Supplementary Fig. 8(g)). However, the entire system would be proportionately more susceptible to tilt between the alignment beam and the DM-scattered signal photons, and likely much less mechanically stable. Achieving a 90% overall SDE (which combines several factors including OCE) would increase the reach of an otherwise equivalent experiment about an order of magnitude in coupling, as illustrated in Fig. 4.

Further improvement can be achieved from background characterization and mitigation. We do not know the source of the observed counts, but for each of the plausible causes, there are mitigation strategies. One possibility is that dark counts arise from intrinsic SNSPD noise processes. When biased close to the switching current, statistical fluctuations in the DC bias current of an SNSPD can seed hotspots near defective or constricted sites along the nanowire length. Recently, it has been demonstrated that SNSPDs with appropriately designed double-ended readouts can be used to spatially resolve dark count sites along the nanowire, suggesting the possibility of vetoing some fraction of false detection events [34].

False counts may also originate from background energy depositions. A simple example is cosmic muons passing through the detector and depositing energy in a way that mimics a photon. Charged particles from radioactive processes may have similar effects. Secondary photons generated by charged particles — for example, Cherenkov photons generated in the lens [35] — are another possibility. We estimate that all of these processes are plausible contributors to the observed dark count rate, and further studies are required to determine which are significant. Possible mitigation strategies include operating underground to reduce the cosmic-ray flux, using more radioactively quiet materials, and using charged particle veto detectors.

Extending the reach to DM masses as heavy as several eV can be achieved by using thin layers of wider-bandgap, high-index materials such as ZnSe or TiO_2 in the dielectric target; SNSPDs with sensitivity to shorter-wavelength photons have already been demonstrated [26]. At frequencies above the bandgap of semiconductor materials, proposed semiconductor detectors such as SENSEI [30, 36, 37], DAMIC [38, 39], and SuperCDMS [40] may be better suited due to their large target volumes.

Turning to lighter DM masses, SNSPDs have demonstrated sensitivity to photon energies as low as $\sim 0.1\,\mathrm{eV}$ ($\lambda \sim 10\,\mu\mathrm{m}$) [25, 41]. Consequently, sensitivity to significantly lighter DM can be achieved using thicker dielectric layers. Since alternative schemes using bulk material excitations may be difficult to realize in the $\sim 100\,\mathrm{meV}$-few eV mass range (between the energy ranges of optical phonons [42] and electronic semiconductor excitations), dielectric haloscopes are well-suited to explore this DM mass range.

By placing the dielectric layers in a magnetic field, axion [43–45] DM with a coupling to photons [46] could also be absorbed, allowing a haloscope to probe axion masses well above the traditional microwave range [16]. If good SNSPD performance in a large magnetic field is achieved (as has been demonstrated in some cases [47, 48]), almost the same experimental setup could be used. If, on the other hand, the SNSPD needs to be in a low-magnetic-field region, an optical configuration that guides the signal photons out of the magnetic field could be implemented using optical fibers.

V. Conclusions

The LAMPOST prototype places the first constraints on dark matter using optical haloscopes, exceeding current constraints in the $0.7-0.8$ eV mass range by up to a factor of 3 in dark photon coupling. At the same time, the prototype demonstrates technologies and techniques that will enable searches over even larger volumes of parameter space. Optimizing the optical collection and detection efficiency of the setup can improve the coupling limits by more than an order of magnitude. Larger volumes of layered dielectric targets, longer integration times, parallel operation of complementary frequency haloscopes, and background characterization and vetoes are all concrete avenues toward a rapid exploration of large regions of dark photon dark matter parameter space. Integration with a large background magnetic field will enable the search for axion dark matter in the eV mass range.

Methods

Construction of the apparatus

The haloscope "core" comprises an aluminum 50 mm optical cage mount, the dielectric stack wafer, and a plano-convex focusing lens epoxied together, with a reflective collimator threaded onto the backside. The core is mounted to Invar posts to minimize thermal contraction, and the posts are mounted to an aluminum baseplate which houses the SNSPD's PCB. The entire haloscope is mounted and housed in a light-tight aluminum enclosure to minimize stray light entering the cryostat through various feedthroughs at higher temperature stages.

The detector is permanently mounted at the three dimensional location of best focus considering the position and orientation of the dielectric stack and the lens. This location is determined by propagating a 635 nm laser from the reflective collimator all the way to the detector. The gold reflector is omitted from an aperture of width $g = 10$ mm in the dielectric stack wafer, allowing the laser to pass through. This allows it to simulate the propagation vector of the DM signal photons. The SNSPD is translated within the plane of the baseplate, and the haloscope core is moved along the focal axis until the alignment beam is visibly focused and centered on the detector area, as viewed through an off-axis microscope and camera setup. Next, the haloscope core is moved closer to the detector by a pre-calculated amount that compensates differences in source properties (wavelength, beam size, beam shape) between the alignment beam and DM signal photons. Finally, the SNSPD is fixed in place with UV-cured epoxy.

Detector characterization

To electrically and optically characterize the fabricated SNSPDs, we designed an experimental setup using a sorption-pump type He-3 cryostat. The haloscope containing the SNSPDs was placed on a 300 mK cold stage. The signal was amplified at the 4 K stage by a cryogenic low-noise amplifier with a total gain of 56 dB and then was sent to a pulse counter. A single mode optical fiber delivered light from 1550 nm and 1700 nm CW lasers into the cryogenic apparatus though a vacuum feedthrough.

An important consideration is whether the apparatus is mechanically stable enough to preserve the intended alignment during the cooldown. A mock haloscope was constructed to independently test this (which used the same SNSPD and PCB). We can detect a misalignment by comparing the experimental and theoretical DE of the SNSPD; a large discrepancy would suggest substantial misalignment. First, we placed a conventional, large-area optical power meter directly above the SNSPD at room temperature and recorded the optical power at a fixed laser power output at 1550 nm. Next, we removed the power meter, cooled the system to 300 mK, and recorded the photon count rate on the SNSPD for the same laser output power (but with a fixed and known optical attenuation added to the signal path to avoid saturating the SNSPD). A DE of 28.3± 0.5% was observed for the case of light polarized along the length of the wire (parallel) and 12.1± 0.5% for the perpendicular polarization. A paddle-type polarization controller was used to shift the state as needed. We simulated the theoretical DE of our detector to be 33.6% for the parallel polarization case and 10.6% for the perpendicular case (see Supplement for details). We note that the experimental parallel DE of 28.3± 0.5% could be 1.117 times higher, or 31.6%, if the SNSPD were operated at a higher bias current (this is necessary to facilitate direct comparison to the simulations, where the internal detection efficiency is assumed to be unity). Comparing the experimental DE of 31.6% (after compensating for incomplete saturation of the internal detection efficiency) to the simulated DE of 33.6% for the parallel polarization case, the magnitude differs only by a factor of 0.94. The discrepancy may be explained by small temporal variations in laser source power, variable scattering loss at fiber connectors at different temperatures, incomplete polarization state purity, and an acceptable amount of misalignment in the beam. The larger-than-expected perpendicular polarization DE and smaller-than-expected parallel DE would be consistent with a slightly impure polarization state during the measurement. We note that the targeting beam changed position by 100 μm in both the lateral directions upon warming up after this mock haloscope test, which was consistent with the behavior of the main haloscope during the actual experiment.

Data collection

Separately, the main haloscope was assembled and tested briefly prior to the data collection. A brief optical measurement at cryogenic temperatures was conducted (without control over polarization), giving a reasonable DE of 19.3% which is between the nominal parallel and perpendicular DE values. Next, the system was warmed to room temperature, and the optical fiber was disconnected to prevent blackbody radiation-induced counts impinging on the detector. After cooling down again, we began recording counts on the main detector over several cycles of the cryostat. At several points, the haloscope was removed from the system, and the optical alignment was inspected to ensure no signif-

icant drift had occurred. A drift of about 100 μm in each axis was observed, consistent with the detailed alignment test conducted separately. We collected count data for both the main and reference SNSPDs over a total time of 180 hours at the 300 mK base temperature.

System detection efficiency calculation

The system detection efficiency (SDE) can be expressed as

$$SDE = OCE \cdot T \cdot DE. \tag{2}$$

The optical collection efficiency (OCE) is derived from ray-tracing simulations of the optical system that incorporate the experimentally observed detector misalignment and realistic properties of the alignment beam. The simulations show that 2.1% of signal photons generated in the stack impinge on the SNSPD in the worst-case misalignment. The transmission coefficient $T = 88\%$ captures a small optical loss incurred by defects in the dielectric stack. Finally, the detection efficiency DE of the SNSPD is the probability of generating a detection event for one photon incident on the detector's footprint; the value is estimated to be 17.5% based on a calibrated measurement of the DE at 1550 nm, which is averaged for both polarization states, followed by an adjustment for 1700 nm photons (the detector is roughly 10% less sensitive at 1700 nm). Overall, we achieve an SDE of 0.32% in our system. More details on calculations and methods can be found in Supplementary Materials.

The OCE constitutes the largest source of loss in our system, and is limited by several factors. First, there is an uncertainty of $\pm 100\,\mu$m in the lateral position of the detector relative to the alignment beam position (observed to vary between cooldowns). Next, the alignment beam does not fill the whole diameter of the focusing lens, which results in a longer Rayleigh length for the beam, making it more difficult to determine the precise location of best focus. Additionally, the lens has considerable spherical aberration, producing a circle of confusion and a significant reduction in power collected by the detector at any particular choice of focal distance. Total internal reflection due to the steep interface of the lens at the outer radius also adds loss.

Conversion rate calculation

There are several measurement uncertainties on the properties of the target, such as the layer thicknesses (discussed in Supplementary Materials). To set conservative limits, we calculate the minimum signal power that is compatible with the possible range of target properties.

This procedure has a non-negligible effect, since the large substrate thickness $t_s \simeq 525 \pm 10\,\mu$m introduces an oscillatory spectral dependence in the signal power. The time-averaged DM absorption rate per unit area, as a function of dark photon mass, is shown in Fig. 3. The blue curve shows the signal power for a target with the measured central value thicknesses and properties. Small variations in target properties can shift the etalon thickness by more than a period, introducing uncertainty in the signal power at a given mass. Analogously, physical variation in e.g. the substrate thickness over the disk results in a disk-averaged conversion power that is averaged over shifted curves. Taking both of these effects into account gives the magenta curve in Fig. 3.

This curve illustrates that our layered target enhances the conversion rate by up to a factor ~ 30 times that of a mirror target [27–29], even taking into account measurement uncertainties. Compared to dark photon absorption in the SNSPD itself, as considered in [23], the much larger area and multiple layers of the dielectric target produce a signal rate from stack-converted photons that is at least $\sim 10^3$ times greater (at its optimum frequencies), despite the small SDE.

Data Availability

All data used in this paper are available from the corresponding author upon reasonable request.

[1] Vera C. Rubin and W. Kent Ford, Jr., "Rotation of the Andromeda Nebula from a Spectroscopic Survey of Emission Regions," Astrophys. J. **159**, 379–403 (1970).

[2] N. Aghanim *et al.* (Planck), "Planck 2018 results. VI. Cosmological parameters," Astron. Astrophys. **641**, A6 (2020), arXiv:1807.06209 [astro-ph.CO].

[3] Michael Dine and Willy Fischler, "The Not So Harmless Axion," Phys. Lett. B **120**, 137–141 (1983).

[4] L. F. Abbott and P. Sikivie, "A Cosmological Bound on the Invisible Axion," Phys. Lett. B **120**, 133–136 (1983).

[5] John Preskill, Mark B. Wise, and Frank Wilczek, "Cosmology of the invisible axion," Physics Letters B **120**, 127–132 (1983).

[6] Peter W. Graham, Jeremy Mardon, and Surjeet Rajendran, "Vector dark matter from inflationary fluctuations," Phys. Rev. D **93**, 103520 (2016).

[7] Raphael Bousso and Joseph Polchinski, "Quantization of four form fluxes and dynamical neutralization of the cosmological constant," JHEP **06**, 006 (2000), arXiv:hep-th/0004134 [hep-th].

[8] Peter Svrcek and Edward Witten, "Axions In String Theory," JHEP **06**, 051 (2006), arXiv:hep-th/0605206.

[9] Asimina Arvanitaki, Savas Dimopoulos, Sergei Dubovsky, Nemanja Kaloper, and John March-Russell, "String Axiverse," Phys. Rev. D **81**, 123530 (2010), arXiv:0905.4720 [hep-th].

[10] Bob Holdom, "Searching for ϵ Charges and a New U(1)," Phys. Lett. **B178**, 65–70 (1986).

[11] Michele Cicoli, Mark Goodsell, Joerg Jaeckel, and Andreas Ringwald, "Testing String Vacua in the Lab: From a Hidden CMB to Dark Forces in Flux Compactifications," JHEP **07**, 114 (2011), arXiv:1103.3705 [hep-th].

[12] S. Dimopoulos and G. F. Giudice, "Macroscopic forces from supersymmetry," Phys. Lett. **B379**, 105–114 (1996), arXiv:hep-ph/9602350 [hep-ph].

[13] T. Damour and Alexander M. Polyakov, "The String dilaton and a least coupling principle," Nucl. Phys. **B423**, 532–558 (1994), arXiv:hep-th/9401069 [hep-th].

[14] Y. Akrami *et al.* (Planck), "Planck 2018 results. X. Constraints on inflation," Astron. Astrophys. **641**, A10 (2020), arXiv:1807.06211 [astro-ph.CO].

[15] Bob Holdom, "Two U(1)'s and Epsilon Charge Shifts," Phys. Lett. **B166**, 196 (1986).

[16] Masha Baryakhtar, Junwu Huang, and Robert Lasenby, "Axion and hidden photon dark matter detection with multilayer optical haloscopes," Phys. Rev. D **98**, 035006 (2018).

[17] Asimina Arvanitaki, Savas Dimopoulos, and Ken Van Tilburg, "Resonant absorption of bosonic dark matter in molecules," Phys. Rev. X **8**, 041001 (2018).

[18] Mark W. Goodman and Edward Witten, "Detectability of Certain Dark Matter Candidates," Phys. Rev. D **31**, 3059 (1985).

[19] Allen Caldwell, Gia Dvali, BÃ©la Majorovits, Alexander Millar, Georg Raffelt, Javier Redondo, Olaf Reimann, Frank Simon, and Frank Steffen (MADMAX Working Group), "Dielectric Haloscopes: A New Way to Detect Axion Dark Matter," Phys. Rev. Lett. **118**, 091801 (2017), arXiv:1611.05865 [physics.ins-det].

[20] Gianpalo Carosi, Raphael Cervantes, Seth Kimes, Parashar Mohapatra, Rich Ottens, and Gray Rybka, "Orpheus: Extending the admx qcd dark-matter axion search to higher masses," in *Microwave Cavities and Detectors for Axion Research*, edited by Gianpaolo Carosi and Gray Rybka (Springer International Publishing, Cham, 2020) pp. 169–175.

[21] B. Phillips, "The electric tiger experiment: a proof-of-concept for the periodic dielectric loaded resonator," in *2nd Workshop on Microwave Cavities and Detectors for Axion Research, Lawrence Livermore National Laboratory* (2017).

[22] James Sloan, "Electric tiger," in *1nd Workshop on Microwave Cavity Design for Axion detection, Livermore Valley Open Campus* (2015).

[23] Yonit Hochberg, Ilya Charaev, Sae-Woo Nam, Varun Verma, Marco Colangelo, and Karl K. Berggren, "Detecting sub-gev dark matter with superconducting nanowires," Phys. Rev. Lett. **123**, 151802 (2019).

[24] Dileep V. Reddy, Robert R. Nerem, Sae Woo Nam, Richard P. Mirin, and Varun B. Verma, "Superconducting nanowire single-photon detectors with 98% system detection efficiency at 1550 nm," Optica **7**, 1649–1653 (2020).

[25] V. B. Verma, B. Korzh, A. B. Walter, A. E. Lita, R. M. Briggs, M. Colangelo, Y. Zhai, E. E. Wollman, A. D. Beyer, J. P. Allmaras, B. Bumble, H. Vora, D. Zhu, E. Schmidt, K. K. Berggren, R. P. Mirin, S. W. Nam, and M. D. Shaw, "Single-photon detection in the mid-infrared up to 10 micron wavelength using tungsten silicide superconducting nanowire detectors," (2020), arXiv:2012.09979 [physics.ins-det].

[26] E. E. Wollman, V. B. Verma, A. D. Beyer, R. M. Briggs, B. Korzh, J. P. Allmaras, F. Marsili, A. E. Lita, R. P. Mirin, S. W. Nam, and M. D. Shaw, "Uv superconducting nanowire single-photon detectors with high efficiency, low noise, and 4 k operating temperature," Opt. Express **25**, 26792–26801 (2017).

[27] Dieter Horns, Joerg Jaeckel, Axel Lindner, Andrei Lobanov, Javier Redondo, and Andreas Ringwald, "Searching for WISPy Cold Dark Matter with a Dish Antenna," JCAP **1304**, 016 (2013), arXiv:1212.2970 [hep-ph].

[28] J. Suzuki, T. Horie, Y. Inoue, and M. Minowa, "Experimental Search for Hidden Photon CDM in the eV mass range with a Dish Antenna," JCAP **1509**, 042 (2015), arXiv:1504.00118 [hep-ex].

[29] Arnaud Andrianavalomahefa, Christoph M. Schäfer, Darko Veberič, Ralph Engel, Thomas Schwetz, Hermann-Josef Mathes, Kai Daumiller, Markus Roth, David Schmidt, Ralf Ulrich, Babette Döbrich, Joerg Jaeckel, Marek Kowalski, Axel Lindner, and Javier Redondo (The FUNK Experiment), "Limits from the funk experiment on the mixing strength of hidden-photon dark matter in the visible and near-ultraviolet wavelength range," Phys. Rev. D **102**, 042001 (2020).

[30] Liron Barak, Itay M. Bloch, Mariano Cababie, Gustavo Cancelo, Luke Chaplinsky, Fernando Chierchie, Michael Crisler, Alex Drlica-Wagner, Rouven Essig, Juan Estrada, Erez Etzion, Guillermo Fernandez Moroni, Daniel Gift, Sravan Munagavalasa, Aviv Orly, Dario Rodrigues, Aman Singal, Miguel Sofo Haro, Leandro Stefanazzi, Javier Tiffenberg, Sho Uemura, Tomer Volansky, and Tien-Tien Yu (SENSEI Collaboration), "Sensei: Direct-detection results on sub-gev dark matter from a new skipper ccd," Phys. Rev. Lett. **125**, 171802 (2020).

[31] J. Angle, E. Aprile, F. Arneodo, L. Baudis, A. Bernstein, A. I. Bolozdynya, L. C. C. Coelho, C. E. Dahl,

L. DeViveiros, A. D. Ferella, L. M. P. Fernandes, S. Fiorucci, R. J. Gaitskell, K. L. Giboni, R. Gomez, R. Hasty, L. Kastens, J. Kwong, J. A. M. Lopes, N. Madden, A. Manalaysay, A. Manzur, D. N. McKinsey, M. E. Monzani, K. Ni, U. Oberlack, J. Orboeck, G. Plante, R. Santorelli, J. M. F. dos Santos, S. Schulte, P. Shagin, T. Shutt, P. Sorensen, C. Winant, and M. Yamashita (XENON10 Collaboration), "Search for light dark matter in xenon10 data," Phys. Rev. Lett. **107**, 051301 (2011).

[32] Haipeng An, Maxim Pospelov, Josef Pradler, and Adam Ritz, "New limits on dark photons from solar emission and kev scale dark matter," Phys. Rev. D **102**, 115022 (2020).

[33] Christopher McCabe, "Astrophysical uncertainties of dark matter direct detection experiments," Physical Review D **82** (2010), 10.1103/physrevd.82.023530.

[34] Qing-Yuan Zhao, Di Zhu, Niccolò Calandri, Andrew E Dane, Adam N McCaughan, Francesco Bellei, Hao-Zhu Wang, Daniel F Santavicca, and Karl K Berggren, "Single-photon imager based on a superconducting nanowire delay line," Nature Photonics **11**, 247–251 (2017).

[35] Peizhi Du, Daniel Egana-Ugrinovic, Rouven Essig, and Mukul Sholapurkar, "Sources of low-energy events in low-threshold dark matter detectors," (2020), arXiv:2011.13939 [hep-ph].

[36] Javier Tiffenberg, Miguel Sofo-Haro, Alex Drlica-Wagner, Rouven Essig, Yann Guardincerri, Steve Holland, Tomer Volansky, and Tien-Tien Yu (SENSEI), "Single-electron and single-photon sensitivity with a silicon Skipper CCD," Phys. Rev. Lett. **119**, 131802 (2017), arXiv:1706.00028 [physics.ins-det].

[37] Michael Crisler, Rouven Essig, Juan Estrada, Guillermo Fernandez, Javier Tiffenberg, Miguel Sofo haro, Tomer Volansky, and Tien-Tien Yu (SENSEI), "SENSEI: First Direct-Detection Constraints on sub-GeV Dark Matter from a Surface Run," (2018), arXiv:1804.00088 [hep-ex].

[38] J. R. T. de Mello Neto *et al.* (DAMIC), "The DAMIC dark matter experiment," *Proceedings, 34th International Cosmic Ray Conference (ICRC 2015): The Hague, The Netherlands, July 30-August 6, 2015*, PoS **ICRC2015**, 1221 (2016), arXiv:1510.02126 [physics.ins-det].

[39] N. Castelló-Mor (DAMIC-M), "DAMIC-M Experiment: Thick, Silicon CCDs to search for Light Dark Matter," Nucl. Instrum. Meth. A **958**, 162933 (2020), arXiv:2001.01476 [physics.ins-det].

[40] T. Aralis, T. Aramaki, I. J. Arnquist, E. Azadbakht, W. Baker, S. Banik, D. Barker, C. Bathurst, D. A. Bauer, L. V. S. Bezerra, R. Bhattacharyya, T. Binder, M. A. Bowles, P. L. Brink, R. Bunker, B. Cabrera, R. Calkins, R. A. Cameron, C. Cartaro, D. G. Cerdeño, Y.-Y. Chang, J. Cooley, H. Coombes, J. Corbett, B. Cornell, P. Cushman, F. De Brienne, M. L. di Vacri, M. D. Diamond, E. Fascione, E. Figueroa-Feliciano, C. W. Fink, K. Fouts, M. Fritts, G. Gerbier, R. Germond, M. Ghaith, S. R. Golwala, H. R. Harris, N. Herbert, B. A. Hines, M. I. Hollister, Z. Hong, E. W. Hoppe, L. Hsu, M. E. Huber, V. Iyer, D. Jardin, A. Jastram, M. H. Kelsey, A. Kennedy, A. Kubik, N. A. Kurinsky, R. E. Lawrence, A. Li, B. Loer, E. Lopez Asamar, P. Lukens, D. MacDonell, D. B. MacFarlane, R. Mahapatra, V. Mandic, N. Mast, É. M. Michaud, E. Michielin, N. Mirabolfathi, B. Mohanty, J. D. Morales Mendoza, S. Nagorny, J. Nelson, H. Neog, J. L. Orrell, S. M. Oser, W. A. Page, P. Pakarha, R. Partridge, R. Podviianiuk, F. Ponce, S. Poudel, M. Pyle, W. Rau, R. Ren, T. Reynolds, A. Roberts, A. E. Robinson, H. E. Rogers, T. Saab, B. Sadoulet, J. Sander, R. W. Schnee, S. Scorza, K. Senapati, B. Serfass, D. J. Sincavage, C. Stanford, M. Stein, J. Street, D. Toback, R. Underwood, S. Verma, A. N. Villano, B. von Krosigk, S. L. Watkins, L. Wills, J. S. Wilson, M. J. Wilson, J. Winchell, D. H. Wright, S. Yellin, B. A. Young, T. C. Yu, E. Zhang, X. Zhao, and L. Zheng (SuperCDMS Collaboration), "Constraints on dark photons and axionlike particles from the supercdms soudan experiment," Phys. Rev. D **101**, 052008 (2020).

[41] Francesco Marsili, Francesco Bellei, Faraz Najafi, Andrew E Dane, Eric A Dauler, Richard J Molnar, and Karl K Berggren, "Efficient single photon detection from 500 nm to 5 μm wavelength," Nano letters **12**, 4799–4804 (2012).

[42] Fabien Tran and Peter Blaha, "Accurate band gaps of semiconductors and insulators with a semilocal exchange-correlation potential," Physical review letters **102**, 226401 (2009).

[43] Steven Weinberg, "A New Light Boson?" Phys.Rev.Lett. **40**, 223–226 (1978).

[44] Frank Wilczek, "Problem of Strong p and t Invariance in the Presence of Instantons," Phys.Rev.Lett. **40**, 279–282 (1978).

[45] R.D. Peccei and Helen R. Quinn, "CP Conservation in the Presence of Instantons," Phys.Rev.Lett. **38**, 1440–1443 (1977).

[46] Peter W. Graham, Igor G. Irastorza, Steven K. Lamoreaux, Axel Lindner, and Karl A. van Bibber, "Experimental searches for the axion and axion-like particles," Annual Review of Nuclear and Particle Science **65**, 485–514 (2015).

[47] T. Polakovic, W.R. Armstrong, V. Yefremenko, J.E. Pearson, K. Hafidi, G. Karapetrov, Z.-E. Meziani, and V. Novosad, "Superconducting nanowires as high-rate photon detectors in strong magnetic fields," Nuclear Instruments and Methods in Physics Research Section A: Accelerators, Spectrometers, Detectors and Associated Equipment **959**, 163543 (2020).

[48] Benjamin J Lawrie, Claire E. Marvinney, Yun-Yi Pai, Matthew A. Feldman, Jie Zhang, Aaron J. Miller, Chengyun Hua, Eugene Dumitrescu, and Gábor B. Halász, "Multifunctional superconducting nanowire quantum sensors," (2021), arXiv:2103.09896 [quant-ph].

[49] M. G. Moharam and T. K. Gaylord, "Rigorous coupled-wave analysis of planar-grating diffraction,"

J. Opt. Soc. Am. **71**, 811–818 (1981).
[50] Frank L Pedrotti, Leno M Pedrotti, and Leno S Pedrotti, *Introduction to optics* (Cambridge University Press, 2017).
[51] "Lambert's cosine law," (2021).

Acknowledgments

MB is supported in part by the James Arthur Postdoctoral Fellowship. RL's research is supported in part by the National Science Foundation under Grant No. PHYS-2014215, and the Gordon and Betty Moore Foundation Grant GBMF7946. Some of the computing for this project was performed on the Sherlock cluster at Stanford. We would like to thank Stanford University and the Stanford Research Computing Center for providing computational resources and support that contributed to these research results. We thank Dr. J. Hilfiker of J.A. Woollam Corp. for providing VASE measurements. We thank Daniel Egana-Ugrinovic and Rouven Essig for useful discussions. Research at Perimeter Institute is supported in part by the Government of Canada through the Department of Innovation, Science and Economic Development Canada and by the Province of Ontario through the Ministry of Colleges and Universities. The MIT co-authors acknowledge support for the later stages of the work from the Fermi Research Alliance, LLC (FRA) and the US Department of Energy (DOE) under contract No. DE-AC02-07CH11359. The initial stages of the work were supported by the DOE under the QuantiSED program, Award No. DE-SC0019129.

Author contributions

J.C., and S.W.N. built the optomechanical apparatus and planned the experimental procedure. I.C, J.C., and M.C. fabricated devices. I.C. and M.C. calibrated and tested the system, and collected the data. R.L., J.C. and I.C. analyzed the data and conducted simulations. M.B., J.H. and R.L. performed theoretical calculations for the design and analysis of the experiment. G.B., A.R., and J.C. contributed to characterization of the stack. M.B., K.K.B., J.C., I.C., J.H., R.L. and S.W.N. contributed to writing of the manuscript. A.A., M.B., K.K.B., J.C., I.C., J.H., R.L., S.W.N. and K.V.T. contributed to project planning. K.K.B. and S.W.N. organized and co-managed the project. All authors contributed to discussions.

Competing interests

The authors declare no competing interests.

Supplementary Materials

A. Dielectric stack fabrication and characterization

The dielectric stack, which is responsible for resonant conversion of DM particles to signal photons, was fabricated at NIST Boulder. The starting substrate was a fused silica wafer 52 mm in diameter, which was mounted with wax to a 150 mm-diameter carrier wafer at the position of best uniformity previously recorded for the deposition system to be used. Prior to film coating, it was plasma-cleaned in oxygen. The dielectric stack was deposited with alternating films of hydrogenated amorphous silicon (a-Si) and silicon dioxide (SiO_2) deposited at 40°C with inductively-coupled plasma chemical vapor deposition (ICP-CVD). Based on measured deposition rates and prism-coupled refractive index measurements, the stack was designed to consist of 5 pairs of 292 nm a-Si and 548 nm SiO_2. A gold reflector with a 5 nm Ti adhesion layer was deposited on top of the last SiO_2 layer with electron beam evaporation.

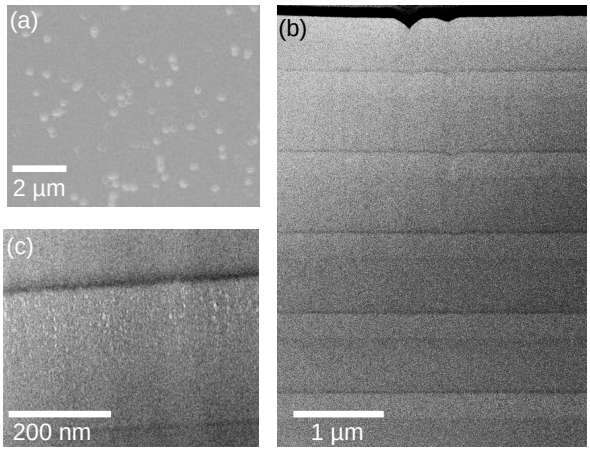

Figure 5. STEM and SEM images of the fabricated stack. (a) Top-view showing numerous small pits occupying a small portion of the surface area. (b) Image of the entire stack, showing one pitted area extending through several layers. (c) High-magnification TEM image of one amorphous silicon layer.

Fig. 5 shows several images acquired through scanning transmission electron microscopy (STEM) and scanning electron microscopy (SEM) of one sample of the fabricated stack. Fig. 5(a) is a top-view image showing the presence of numerous small (0.1 μm^2 area) pits present on the sample. These do not typically extend down to the bottom layer (as seen in 5(b)), but nevertheless we assume that no signal is generated from the area of the stack intersecting

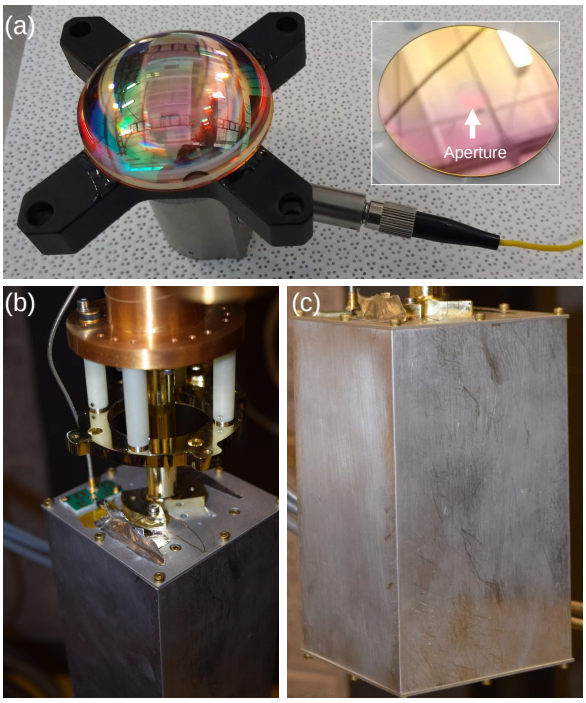

Figure 6. (a) Assembled haloscope core with fiber collimator. Inset: backside of dielectric stack prior to core assembly. (b) A haloscope enclosure mounted on the 300 mK stage of cryostat. (c) View of light-tight enclosure.

with any blisters, resulting in a stack transmission coefficient of 0.88 (or 12% loss) which factors into the final SDE calculation. Small interface effects were also observed between layers, which may be a consequence of sputtering damage or interdiffusion during the early stages of each layer's deposition.

The precise layer thicknesses were determined with variable-angle spectroscopic ellipsometry over a wavelength range from 200 - 1700 nm. The refractive index of each type of film (such as a-Si or SiO_2) was fitted over all measured data but assumed to be constant for all layers. Layer thicknesses were left uncoupled to allow for interlayer thickness variability. Experimentally, we observed actual thicknesses of 590 nm, 591 nm, 593 nm, 591 nm, and 595 nm for the SiO_2 layers (starting at the gold reflector and moving toward the substrate), and 289 nm, 282 nm, 286 nm, 280 nm, and 288 nm for the a-Si layers in the same order. Considering two samples from different areas on the wafer, a variability of $< \pm$ 0.2% was observed, which has a negligible effect on the stack's behavior. The overall bias toward thicker-than-intended SiO_2 layers may have resulted from different deposition behavior for the fused silica wafer which was wax-mounted to a silicon carrier wafer. The near-infrared refractive index of the a-Si layer was determined to be 2.64, and the refrac-

tive index of the SiO_2 layer was 1.48. Both indices are constant over the mirror's response range. The imaginary components of the refractive indices were previously measured to be $< 10^{-4}$ in the wavelength range of interest to this experiment, making them negligible for the optical performance of the stack.

B. Optical simulations

The OCE calculation heavily influences the sensitivity of LAMPOST through its effect on the SDE. In this section, we will explain in greater detail the calculations and methodology involved in arriving at the final numbers for the OCE. We chose to analyze the optical system with non-sequential ray tracing, which efficiently captures the effects of many aberrations and misalignment effects present in the physical system.

In particular, it is useful to understand the relationship between the alignment beam (to point the dielectric stack at the detector) and the DM signal that would hypothetically be produced inside the stack. The aperture in the stack gives an annulus source shape for the DM signal and a circular beam profile for the alignment beam. Because of spherical aberrations and chromatic focal shift, these two beams do not share the same focal distance. In the laboratory setting, the alignment beam can be observed to pass through a focus on the plane of the detector by moving the haloscope core (lens, stack, collimator). If we replicate the system parameters (lens shape, source properties such as profile, wavelength, etc) in a ray tracing model, we can also obtain an equivalent position of best focus, shown in Fig. 7(a) as z_{align}. It need not be in exactly the same position as the experimentally observed focal distance. Next, in the ray tracing model, we change the source properties to mimic the expected DM signal, which is an annulus with a beam diameter of $d = 52$ mm and a circular stop the same diameter as the aperture $g = 10$ mm, emitting at 1550 nm (Fig. 7(b)). The new position of best focus for the DM signal is found at a displacement of dz_{signal}, or -1 mm (negative values being closer to the detector plane) in our case. The effect of thermal contraction in the invar cage rods supporting the haloscope core was also included in this number. Knowing dz_{signal}, we can use it during the experiment by first locating the visible focus for the 635 nm alignment beam, then moving the haloscope core closer to the detector by 1 mm. Note that the signal sources were simulated with zero intial beam divergence (in contrast to the 10^{-3} rad angular opening expected for a DM-converted signal photon) since aberrations and misalignment always produced larger simulated spot sizes than if it were limited by this factor.

Next, ray tracing is used to calculate the estimated OCE for the system when it is aligned at this position, for the peak signal wavelength of 1700 nm (note this differs from the expected wavelength of 1550 nm due to larger-than-intended layer thicknesses). We identified two sources of misalignment that are sufficiently large to consider in this estimation, which are defocus (deviation from the best focal length in the z axis) and unwanted detector translation along the xy plane away from the calculated DM signal spot position. We estimate a defocusing error of $\pm$ 2 mm in our experiment. The translation error constitutes a fixed and known misalignment contribution as well as a systematic uncertainty. The fixed misalignment itself comes from (i) off-axis tilt in the reflective collimator, causing the alignment beam position to differ from the DM signal position by a small amount, and (ii) an initial error in the detector position when it was glued down, due to shifting during the curing of the epoxy used to fix it in place. Both these values were summed and used in the ray tracing simulations shown in Fig. 8 as a starting location for the DM signal beam's position relative to the detector. We noted that the alignment beam's position in the plane of the detector was observed to vary by $\pm$ 100 μm when inspected between cooldown cycles. As there is no reason for this error to vary during data collection once the apparatus has cooled to ~300 mK, and since we cannot inspect the alignment beam's position when

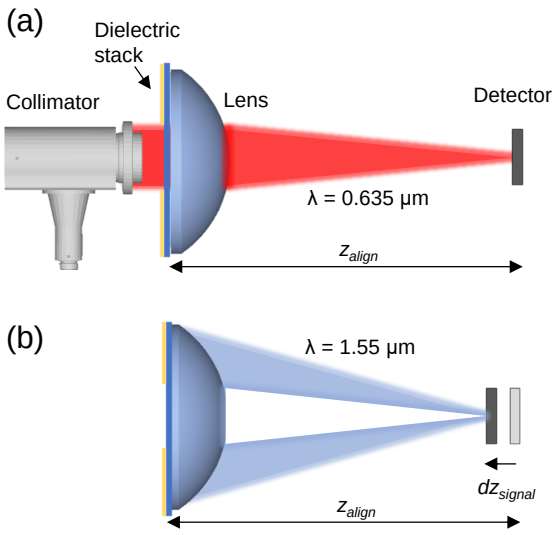

Figure 7. Optical system used in ray-tracing and alignment planning. (a) Propagation of the red alignment beam through the aperture, resulting in a position of best focus z_{align} for the detector during the initial alignment. (b) Effective behavior of the DM signal photon source as an annulus with a modified position of best focus ($z_{align} - dz_{signal}$).

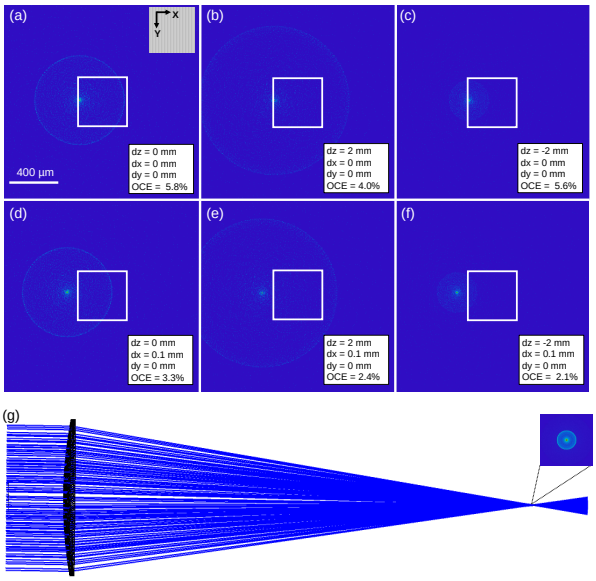

Figure 8. (a-f) Non-sequential ray tracing results for various misalignment configurations, showing ray intercepts at the plane of the detector. Fifty-thousand rays were used for ray-tracing. The detector's active area is indicated by the white boxes. Coloration represents incoherent intensity on the plane of the detector determined by ray intercepts. Inset: coordinate system used for displacements. (g) Ray tracing of the improved optical design using a longer focal length lens which achieves 93% OCE. Inset: Ray intercepts at the detector plane for the improved design.

cooled down, we incorporated this as a systematic uncertainty to be tested for worst-case estimation of the OCE. Ray tracing simulations were performed to compare several plausible misalignment scenarios Fig. 8(a-f). In the top row, it can be seen that the OCE is $> 4\%$ regardless of the defocus value when there is no additional systematic displacement of the detector relative to the signal beam (note that a fixed displacement is always included, considering the experimentally observed imperfect initial alignment of the detector area). However, in the bottom row, we assume the worst case situation in which the detector is shifted relative to the signal beam by $+100$ μm along the x-axis, sending much of the beam off of its surface. On top of this, the defocus is varied as usual, resulting in the worst-case OCE estimation of 2.1% in Fig. 8(f). We note that displacement in the y-axis does not significantly affect any of the results, within the tolerance observed. As a final note, we neglected the influence of signal light transmitted through the aperture portion of the stack, where the reflector is absent.

We also simulated a hypothetical case in which the detector was optimally aligned and positioned at the best focus without positional uncertainty, which achieved an OCE of 9.4%, showing that considerable improvements are possible by refining the alignment and mounting techniques. Finally, we note the ray tracing results for a modified haloscope optical path (Fig. 8(g)) which uses a plano-convex lens of a much larger focal distance (200 mm) with the convex side facing the stack. These changes would minimize the effects of spherical aberration and total internal reflection losses, resulting in a significantly improved OCE of 93%.

We also conducted optical simulations of the SNSPD's detection effciency under various conditions for the purpose of validating our alignment strategy and confirming nominal operation of the SNSPD. We conducted a combination of 2D finite-element modeling and rigorous coupled-wave analysis [49] to obtain this value, using the best available measurements of material thicknesses, refractive indices, and lateral dimensions of the as-fabricated SNSPD. Considering only the light incident from the top surface of the SNSPD, the theoretical detection efficiency is 32.7% for the parallel polarization (and 10.2% for the perpendicular polarization). However, given the large detection area of this device and the size of the near-infrared beam used for alignment, the reflection off the backside of the silicon substrate cannot be neglected in the calculation of the total absorption coefficient in the detector. This factor is most significant when the beam is centered on the detector area but focused on the bottom surface of the substrate. Conservatively, if we assume the worst case in which the focal spot of the beam is centered on the detection area and focused on the bottom side of the substrate, the light transmitted through the SNSPD will diffusely scatter off the unpolished back silicon surface with a Lambertian intensity profile. The total absorption coefficient of this backward pass can then be calculated by integration of light scattered to angles encompassing the SNSPD's active area, and multiplication by the angle-dependent absorption coefficient of the SNSPD for light incident from underneath, referred to as the backward pass. For simplicity, we neglect light scattered into the perpendicular polarization, which has a much smaller absorption coefficient. Light scattered under a Lambertian profile has a radiant intensity proportional to the cosine of the angle between the incident beam and the surface normal [50]. We start with the calculation of radiant flux F_{tot} emitted from a Lambertian surface [51]:

$$F_{tot} = 2\pi I_{max} \int_b^c \frac{\sin(2\theta)}{2} d\theta,$$

where θ is the angle of incidence, b and c are the angular span of integration, and I_{max} is is the peak

radiant intensity chosen as $1/\pi$ so that $F_{tot} = 1$ when integrating θ from 0 to $\pi/2$, the full angular range available in reflection. To calculate the angular dependence of the total absorption in the detector during the backward pass, we include the angular dependence of the detector's absorption coefficient in the integral of the previous expression, and integrate over the angles of incidence in which the detector is visible to the point of reflection:

$$\alpha_{bkwd} = 2\int_0^{\Omega} \frac{\sin(2\theta)}{2}\alpha(\theta)d\theta,$$

where α_{bkwd} is the total absorption coefficient of the backward pass, $\alpha(\theta)$ is the angle-dependent absorption coefficient of the detector from backward incidence (around 21% for relevant angles, obtained from 2D simulations), and Ω is the maximum angle of incidence where the detector area is still visible to the reflected beam (0.49 rad). We calculate α_{bkwd} to be 4.9%. Next, we consider that only some of the original light incident on the top surface remains at the point of reflection off the back surface. The transmission coefficient through the detector, T, is 0.62, and the reflection coefficient R off the back surface is estimated to be uniformly 0.306, which when multiplied together and with α_{bkwd} result in an effective increase in the DE of about 1% due to the backward pass. Adding this to the forward-pass DE, the total detection efficiency of the SNSPD is estimated to be 33.6% in the case of an incident beam perfectly aligned to the detector area, and polarized parallel to the nanowire's long axis. For the case of the perpendicular polarization, the backward pass has a marginal influence, increasing the total DE from 10.2% to about 10.6%. We ignore the effect of light scattered into the rest of the substrate, since the 1 cm^2 die is large enough that most of the captured light will escape before encountering the relatively small detector area again.

C. SNSPD fabrication and testing

The device was fabricated from 7-nm thick WSi film which was sputtered on a 150 nm thick thermal silicon oxide film on a silicon substrate at room temperature with RF co-sputtering. Additionally, a thin 2-nm Si layer was deposited on top of the WSi film in-situ to prevent oxidation of the superconductor. To pattern the nanowires, electron-beam lithography was used with high-resolution positive e-beam resist. The ZEP 520 A resist was spin coated onto the chip at 5000 rpm which ensured a thickness of 335 nm. After exposure, the resist was developed by submerging the chip in O-xylene for 80 s with subsequent rinsing in the 2-propanol stopper. The ZEP 520 A pattern was then transferred to the WSi by reactive ion etching in CF_4 at 50 W for 5 minutes. The ZEP thickness is estimated to be 250 nm after etching and is left on the top surface.

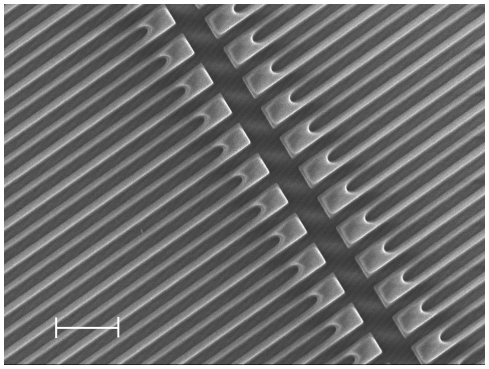

Figure 9. Scanning electron micrograph of nanowires after fabrication. Scale bar: 1 μm

Fig. 9 is a scanning electron micrograph (SEM) of the tungsten silicide (WSi) SNSPD after fabrication. The device area was 400 by 400 μm^2, and the nanowire was connected to external circuitry via two contact pads. The width of the nanowires was 140 nm with a pitch of 340 nm.

The switching current of the detector I_C was 5.5 μA measured at 300 mK by sweeping the current from a 50 Ω impedance source. Fig. 11 shows the dependence of the count rate on the absolute bias current for 400 by 400 μm^2 large-area SNSPD at 1550 nm wavelength (~0.8 eV). When the detector was illuminated, the count rate (open red dots) rose at a bias current of 3 μA. Counts initially grew with the current and the device was nearly saturated at a bias

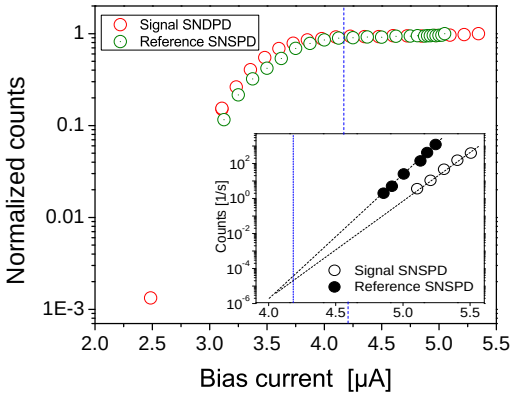

Figure 10. Normalized count rate as a function of the absolute bias current measured at 1550 nm for the primary SNSPD and reference SNSPD with identical geometry. Inset: DCR as a function of the bias current taken from both detectors.

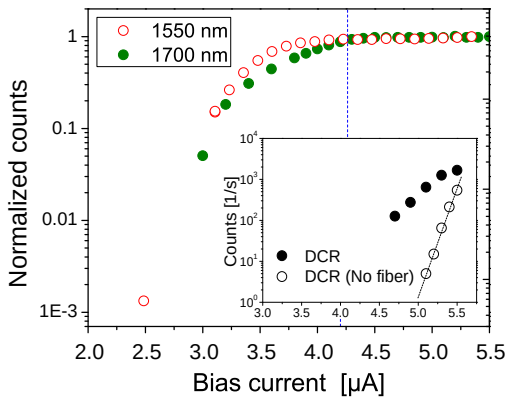

Figure 11. Normalized count rate as a function of the absolute bias current measured at 1550 nm (open red dots) and 1700 nm (green dots) wavelengths. Data was taken at 300 mK of bath temperature. The SNSPDs show pronounced saturation at both wavelengths. Inset: Comparison of DCRs with optical fiber connected (filled circles) and disconnected (open circles).

current of 4.2 μA. At this bias current, the count rate with the laser light turned off (background count rate) was below 100 counts/s. The maximum background count rate (black dots) was measured at a point just below the switching to the normal state, at 10^3 counts/s. The open dots represents background count rate when fiber was decoupled from haloscope. Blocked infrared photons result in significant reduction of background noise. With extrapolation of experimental data, the expected count rate at the working bias current (shown by dashed blue line) for the long-duration integration experiment is $\sim 10^{-4} - 10^{-5}$ Hz.

D. Confidence limits on DM coupling

As discussed in Section III, over the total 180 hour exposure, the experiment's reference SNSPD registered 5 counts, while the haloscope detector registered 4 counts (Fig. 12). To make a precise statistical statement about the DM coupling, given these observations, we can assume that the reference and haloscope counts, N_r and N_h (viewed as random variables), are independent and Poisson-distributed, with means s_n and $s_n + s_A$ respectively, where s_n is the expected number of dark counts and s_A is the expected number of DM signal counts (for a given DM coupling). As our test statistic, we take the joint likelihood for seeing the observed numbers of counts n_r and n_h, and ask (for some particular assumed s_n and s_A) how probable it is to obtain a test statistic as small or smaller than that for the observed values $n_r = 5$, $n_h = 4$ (we take a one-sided test, only

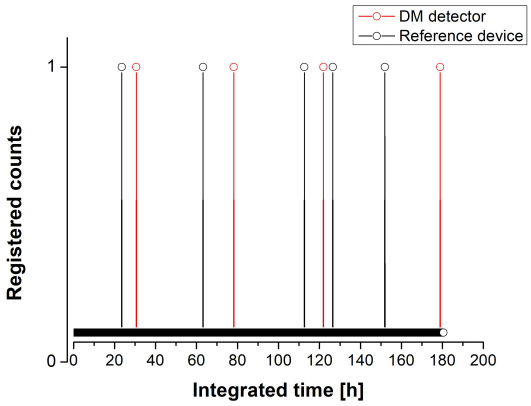

Figure 12. Experimental results of long-duration integration experiment with large-area SNSPDs mounted into a haloscope. Red points correspond to the signal obtained from a device aligned with the lens, while black points show counts taken from a reference detector placed far from focus of the target.

considering $n_h < s_n + s_A$, since we are interested in scenarios where the DM count is abnormally low, despite there being a signal). For example, if we take $s_A = 5$, then this probability is maximised by taking $s_n \simeq 3.3$, obtaining a maximum value $\simeq 0.1$. Consequently, the 90% limit on the DM coupling is set by the coupling value that gives 5 expected events.